Electronic Supplementary Information (ESI) for *Energy & Environmental Science*.

An electric double layer regulator empowers robust solid-electrolyte interphase for potassium metal batteries

Xueyu Lian[1†], Liang Xu[2†], Zhijin Ju[3†], Ziang Chen[1], Xiaopeng Chen[1], Yuyang Yi[4], Zhengnan Tian[5], Tao Cheng[2]*, Shixue Dou[6], Xinyong Tao[7]*, & Jingyu Sun[1,8]*

1. *College of Energy, Soochow Institute for Energy and Materials Innovations, Key Laboratory of Advanced Carbon Materials and Wearable Energy Technologies of Jiangsu Province, Soochow University, Suzhou 215006, P. R. China. E-mail: sunjy86@suda.edu.cn*
2. *Institute of Functional Nano & Soft Materials, Jiangsu Provincial Key Laboratory for Carbon-Based Functional Materials & Devices, Joint International Research Laboratory of Carbon-Based Functional Materials and Devices, Soochow University, Suzhou 215123, China.*
3. *College of Chemistry and Materials Engineering, Wenzhou University, Wenzhou 325035, China.*
4. *Department of Industrial and Systems Engineering, The Hong Kong Polytechnic University, Hong Kong 999077, China.*
5. *College Physical Sciences and Engineering Division, King Abdullah University of Science and Technology, Thuwal 23955-6900, Saudi Arabia.*
6. *Institute of Energy Materials Science, University of Shanghai for Science and Technology, Shanghai 200093, P. R. China.*
7. *College of Materials Science and Engineering, Zhejiang University of Technology, Hangzhou 310014, China.*
8. *Beijing Graphene Institute, Beijing 100095, China.*

†These authors contributed equally to this work.

Experimental Section

Sample Preparations

Fabrication of SG@GF:

S-doped graphitic carbon carpet was prepared on the surface of commercial glass fiber (GF) *via* a plasma-enhanced chemical vapor deposition (PECVD) strategy. In detail, a GF sheet with a size of 20 mm × 100 mm was placed in a quartz boat, which was subsequently positioned in the center of a horizontal quartz tube. The CVD system was pumped to a base pressure of 3 Pa and then purged with 20 standard cubic centimeters per minute (sccm) Ar. The system was heated to a growth temperature of 600 ℃ within 30 min, followed by introducing 15 sccm thiophene as the carbon source. Meanwhile, switching on the plasma with 80 W initiated the synthesis of SG for 40 min. After that, the furnace was cooled down to room temperature under Ar. Subsequently, the thus-prepared material was subject to a gentle air plasma treatment (80 W, 40 s) only on the rear side of GF to remove the grown graphene for avoiding short circuits.

Fabrication of MOH-SG@GF:

The obtained SG@GF was placed into a Teflon-lined stainless-steel autoclave. $Co(NO_3)_2·6H_2O$ (1.17 g) and 2-methylimidazole (2-MeIm; 2.60 g) were respectively dissolved into 80 mL deionized water to form two solutions, which were then mixed and stirred at room temperature for 5 min. The mixture solution was subsequently poured into the autoclave and kept at 120 ℃ for 5 h to allow the hydrothermal reaction. Upon cooling, the Co-based MOH-SG@GF material was rinsed for several times with deionized water to remove the residual precipitation and dried at 60 °C. The synthetic procedure of MOH(Fe)-SG@GF or MOH(Ni)-SG@GF was identical except for the substitution of $Co(NO_3)_2·6H_2O$ with $Fe(NO_3)_3·9H_2O$ (1.62 g) or $Ni(NO_3)_2·6H_2O$ (1.17 g).

Preparation of PTCDA cathode:

The commercial perylene-3,4,9,10-tetracarboxylic dianhydride (PTCDA, J&K Scientific) was annealed at 450 °C for 4 h under an Ar atmosphere with a heating rate of 5 °C min^{-1}. The cathode was prepared by mixing PTCDA with SuperP carbon and polyvinylidene fluoride (PVDF) at a weight ratio of 7:2:1 by using N-methyl pyrrolidone (NMP) as the solvent. After stirring for 2 h, the homogeneous slurry was casted onto an aluminum (Al) foil and dried at 80 °C for 24 h. The material was finally cut into disc with a diameter of 12 mm and a mass loading of 1.0 mg cm^{-2} for full-cell assembly.

Characterizations

The morphology of the as-prepared samples was observed by using Hitachi SU8010 scanning electron microscopy (SEM). XRD test (including *operando* mode) was operated with a Cu-Kα radiation. Raman spectroscopy (including *operando* mode) was operated through an excitation wavelength of 532 nm. *In situ* optical microscopy (YUESCOPE YM710R) was carried out to observe the dendrite growth. The elemental

composition and bonding configuration of SEI were analyzed using XPS with an Escalab 250Xi Spectrophotometer. All electrodes were washed with anhydrous DME to remove residual electrolyte and then dried inside a glove box.

Electrochemical measurements

Coin-type (CR2032) cells were assembled inside an Ar-filled glove box with K metal serving as the electrode. The asymmetric Al‖K cells, symmetric K‖K cells and full cells were assembled using different separator materials with an electrolyte of potassium bis(fluorosulfonyl)imide (KFSI) in dimethoxyethane (DME) without any additives. Galvanostatic charge/discharge profiles, rate and cycling performance tests were carried out on LAND CT2001A battery testing system under an ambient temperature. Prior to testing, Al‖K cells underwent a formation process within a voltage range of 0–1 V at a current density of 0.05 mA cm^{-2}. Asymmetric Al‖K cells were cycled by alternately plating/stripping with a deposition time of 1 h and stripped voltage of 1.0 V. Galvanostatic cycling and rate capability measurements based on symmetric K‖K cells were carried out through charge/discharge for 1 h. The full cells were tested at a voltage range of 1.5–3.5 V. EIS, Tafel and LSV curves were recorded using a CHI660E electrochemistry workstation.

The ionic conductivity was tested by inserting different separators between two stainless steel (SS) pieces. EIS was then performed with an amplitude of 5 mV. The ion conductivity was calculated by the Equation (S1):

$$\sigma = \frac{L}{R_b * A}$$

(S1)

where σ is the K$^+$ conductivity, L is the thickness of the separator, R_b is the bulk resistance, and A is the area of the SS electrode.

K$^+$ transference number (t_{K+}) was derived from EIS and chronoamperometry (CA) tests based on symmetric cell configurations. The t_{K+} could be obtained from the Equation (S2):

$$t_{K+} = \frac{I_S(\Delta V - I_0 R_0)}{I_0(\Delta V - I_S R_S)}$$

(S2)

where I_0 and I_S indicate the initial current and steady state current, measured before and after applying polarization, respectively. R_0 and R_S denote the cell resistance value measured before and after undergoing polarization, respectively.

The activation energy (E_a) could be calculated based on the Arrhenius Equation (S3):

$$k = A exp(-\frac{E_a}{RT})$$

(S3)

where k is the rate content, R represents molar gas constant [8.314 (J/(mol·K)] and T indicates thermodynamic temperature.

The equation can be simplified as below:

$$\frac{1}{R_{SEI}} = A exp(-\frac{E_a}{RT})$$

$$\frac{1}{R_{ct}} = A exp(-\frac{E_a}{RT})$$

(S4)

R_{SEI} and R_{ct} was derived from the equivalent circuit model.

The average CE was determined from the Aurbach method. Specifically, the Al‖K cells were cycled under 0.5 mA cm^{-2}/0.5 mAh cm^{-2} and finally fully stripped to 1.0 V. The average CE obeys the following relation:

$$Average\ CE = \frac{nQ_C + Q_S}{nQ_C + Q_T}$$

(S5)

where nQ_C is the cumulative cycling capacity, Q_S is the fully stripped capacity and Q_T is the pre-deposited capacity.

Simulation details

Model building: To calculate the binding energy between $Co(OH)_2$ and sulfur-doped graphene, C atoms were replaced by S atoms in a single layer of graphene to form doped graphene. The single layer of graphene was built with a $(2 \times 4 \times 1)$ unit cell, and a vacuum thickness was set at 20 Å to remove any interaction between the periodic slab. $Co(OH)_2$ was placed over the S atom. To demonstrate the graphene growth on the glass-based separator through chemical reaction, the main component of the separator is SiO_2, thus an amorphous SiO_2 surface was employed. The corresponding graphene was modeled with a $(10 \times 6 \times 1)$ unit cell, which was placed on the SiO_2 surface. The combined model was built using PACKMOL[1, 2]. The simulation of an EDL involved the consideration of both electrode and electrolyte. As for the electrode, a (110) plane of K metal was cleaved to act as the electrode, which was modeled with a $(5 \times 6 \times 4)$ unit cell. As for the electrolyte, 4.0 M KFSI-DME was built consistent with experiments over the electrode as the reference system, which included 289 KFSI and 695 DME in a $(3.2 \times 3.8 \times 15.0\ nm^3)$ cubic box. As for introducing the $Co(OH)_2$ as a valid component on the separator, 10 $Co(OH)_2$ were inserted into the electrolyte, where the amount of KFSI and DME remained the same as the reference system. These initial EDL structures were also constructed using PACKMOL.

DFT calculations: Adsorption energy computation for $Co(OH)_2$ on sulfur-doped graphene were performed using Vienna *ab initio* Simulation Package (VASP) with the projector augmented wave (PAW) method and a plane wave basis set. The method was DFT with generalized gradient approximations (GGA) of Perdew-

Burke-Ernzerhof (PBE) functional. A dispersion correction, DFT-D3 method with Becke-Jonson damping, was included in the calculations. The energy cut-off was set at 400 eV. Reciprocal space was sampled by Γ-centered Monkhorst-Pack scheme with a grid of $3 \times 3 \times 1$. Spin polarization did not have an appreciable effect on the overall energies and was not included. The partial occupancies for each orbital were set with the first order Methfessel-Paxton scheme in the smearing width of 0.2 eV. The dipole moment corrections for the total energy were considered in the direction normal to the surface. The self-consistent electronic step was considered converged when the total energy change and eigenvalues change between two steps were both smaller than 10^{-5} eV. A conjugate-gradient algorithm was used to relax the ions in energy minimization. The minimization was considered converged when all the atomic force was smaller than 0.01 eV/Å, where convergence to an energy minimum. Graphene includes none-S doped, one S atom doped (S_1), two S atom doped (S_2) and three S atom doped (S_3) types, where the adsorbed energy was computed based on the following equation:

$$\Delta E_{binding} = E_{Co(OH)_2@S@graphene} - E_{Co(OH)_2} - E_{S@graphene} \tag{S5}$$

Note that the FSI⁻, DME, MOH-FSI⁻, MOH-DME were optimized by Gaussian 16 at a level of B3LYP with the 6-31G(d) basis set for all atoms. The optimized molecular structures could be used for analyzing HOMO-LUMO using Gaussian view.

ReaxFF MD simulations: The parameters of Reax force field were obtained from work of a previous study[3]. LAMMPS 2018.12 was employed as the simulated tool. The process includes energy minimization and 50 ps NVT simulation. The time-step was 0.5 fs; the temperature was set at 493.15 K (873.15 K); and the atoms in the bottom below 10 Å were fixed during simulation. Moreover, the bottom and top were also set an elastic wall for avoiding atoms to cross over the boundary.

Classical MD simulations: The force field of DME, K⁺, FSI⁻, Co²⁺, OH⁻, K metal species was OPLS-AA under further optimization. In the initial force field, the charges of above species were 0.8, –0.8, 1.6, –0.8 and 0, respectively. The significant non-bond parameters include sigma and epsilon, representing interaction of repulsion and attraction in force field (Table S5–S8). The constant charge potential simulations were also carried out for the reference and Co(OH)₂ systems, where the constant charge potential was accomplished by setting the charge density of the electrode, which was –11.6 μC cm⁻², hence –0.146735 e was assigned to each K atom in the first layer of the electrode close to the electrolyte, and additional 11 K ions were added into the electrolyte for keeping the system at a neutral state. GROMACS 2020.3 was selected as the simulated toolbox[4], where the simulated process includes energy minimization and 10 ns NVT. The time-step was set at 1 fs; the temperature was set at 298 K. The cutoff radius for Coulomb interaction and vdW was 1.0 nm. The long-range Coulomb interaction was calculated by PME method[5] and long-range correction was taken into vdW energy and pressure. K metal electrode was employed position restraint for keeping the electrode stable using huge force constant 10^6 kJ/mol nm² in three directions.

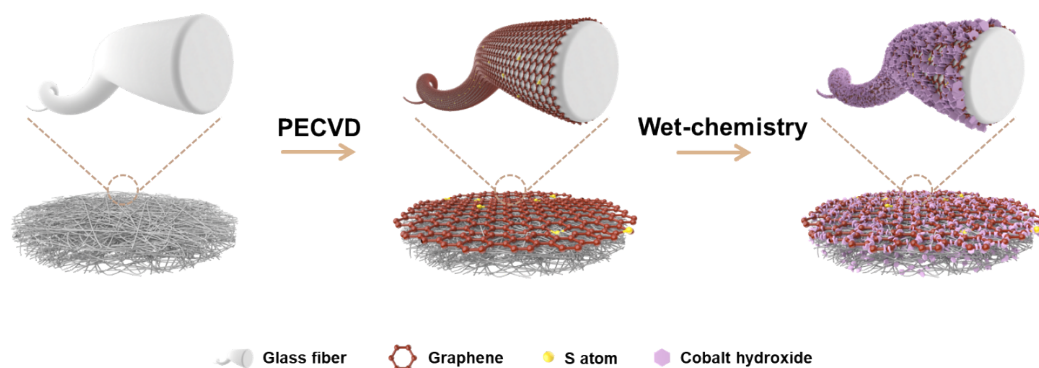# Supplementary Figure and Table

Fig. S1: Schematic illustrating the fabrication of the MOH-SG@GF separator. This strategy involves the S-doped graphene modification *via* a PECVD route and MOH decoration through a wet-chemistry process. The fabrication of $Co(OH)_2$ is serving as a representative.
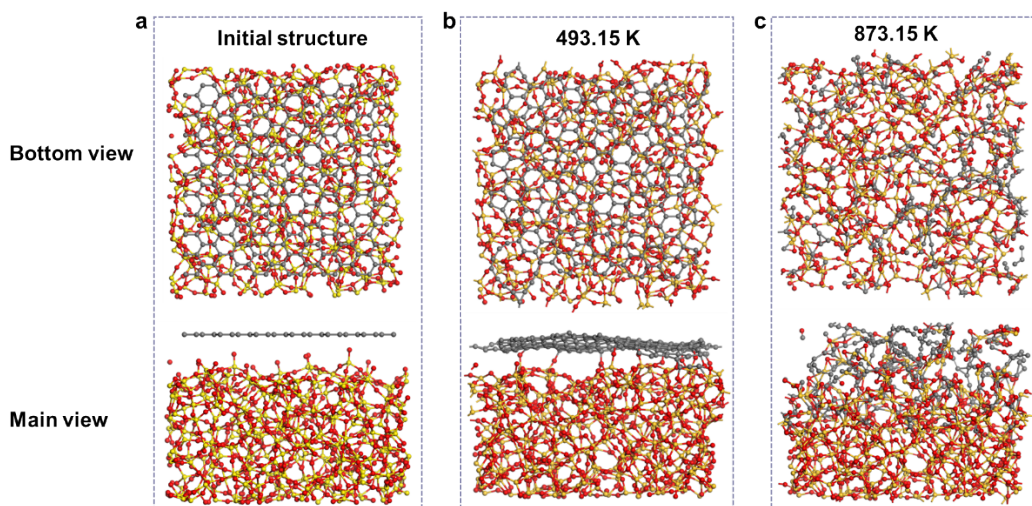

Fig. S2: MD simulations toward the interaction between graphene and glass. Snapshots of reaxFF MD simulation on graphene and SiO_2 under (a) initial, (b) 493.15 K and (c) 873.15 K, respectively.
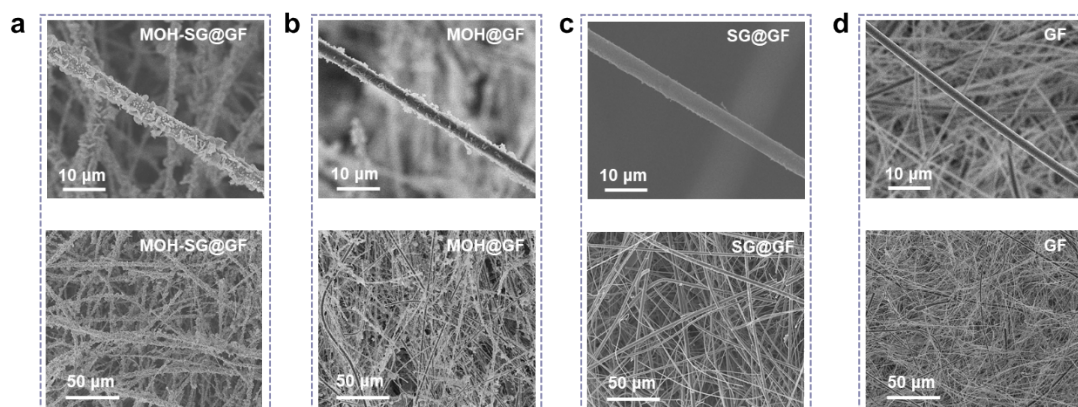
Fig. S3: Surface morphologies of separator materials. Low-magnification SEM images of (a) MOH-SG@GF, (b) MOH@GF, (c) SG@GF and (d) GF.
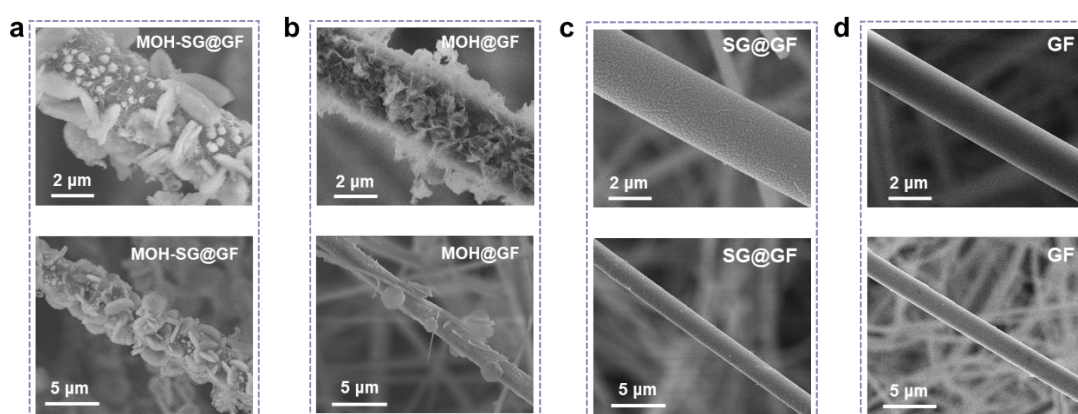
Fig. S4: Surface morphologies of separator materials. High-magnification SEM images of (a) MOH-SG@GF, (b) MOH@GF, (c) SG@GF and (d) GF.
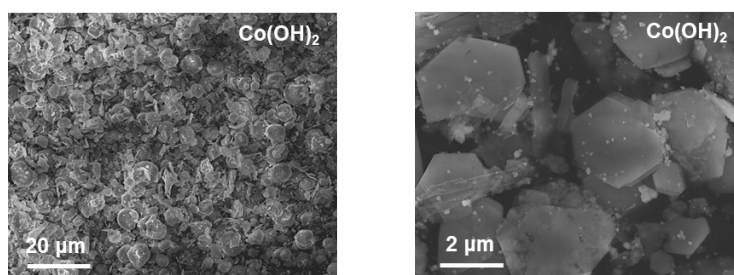
Fig. S5: SEM images of bare $Co(OH)_2$ powder.
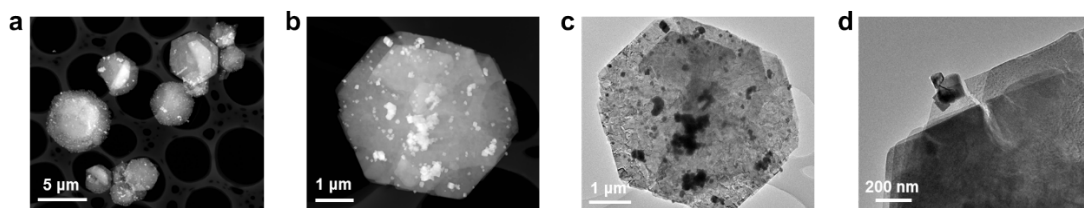
Fig. S6: Detailed morphologies of MOH. (a−c) Low- and (d) high-magnification TEM images of Co(OH)$_2$ powder.
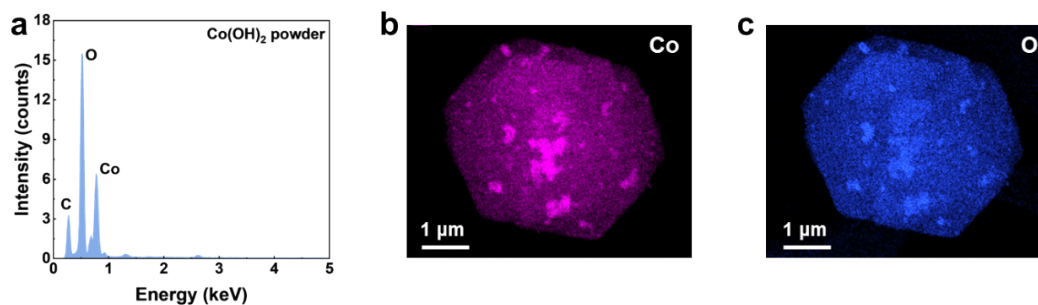
Fig. S7: Elemental information of MOH. (a) EDS profile and (b,c) elemental maps of Co(OH)$_2$ powder.
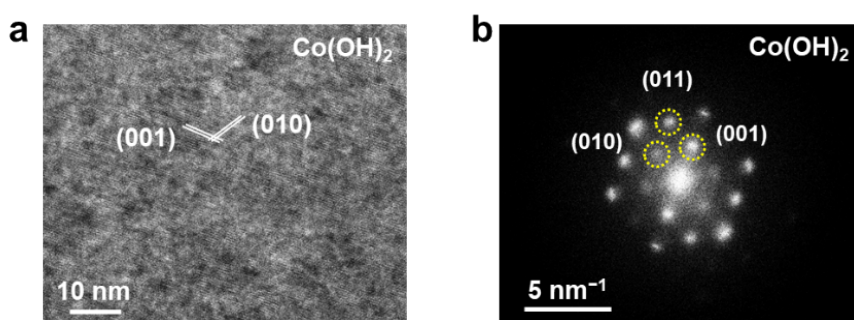
Fig. S8: Crystallographic analysis of MOH. (a) High-resolution TEM image of Co(OH)$_2$ powder and (b) corresponding FFT pattern.
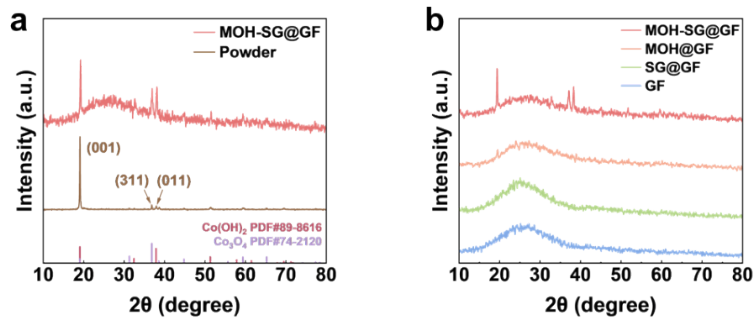
Fig. S9: XRD patterns of (a) $Co(OH)_2$ and (b) modified separator materials.
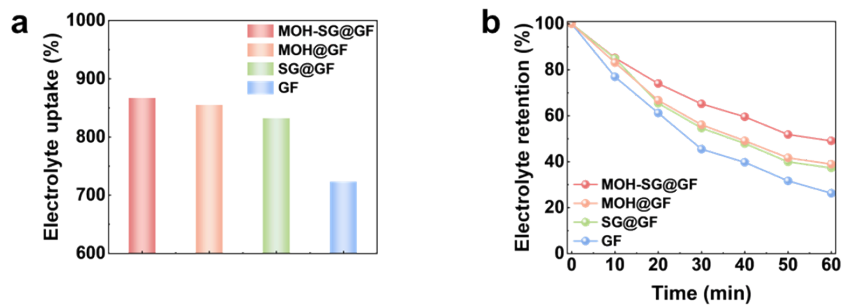
Fig. S10: (a) Electrolyte uptake and (b) electrolyte retention of different separators.
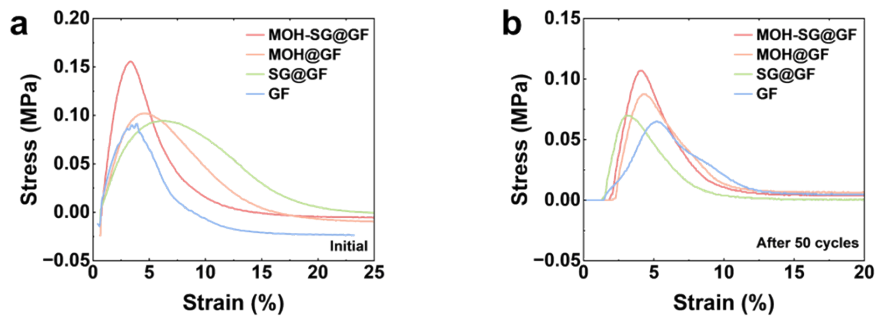
Fig. S11: Mechanical property analysis. Stress-strain curves of tested samples experiencing (a) separator modification and (b) electrochemical cycling.
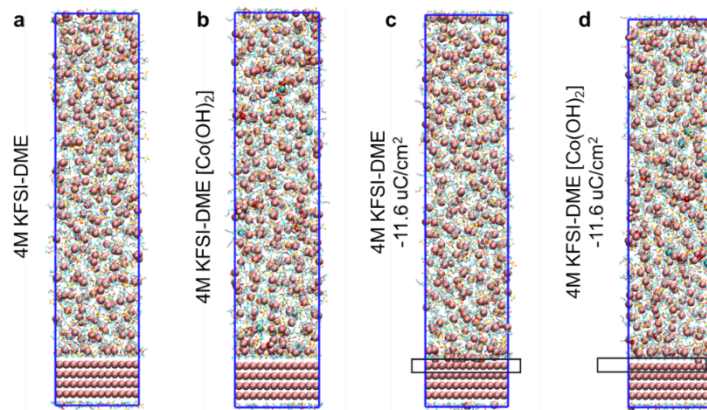
Fig. S12: MD simulations on EDL. Snapshots of MD simulations on EDL of 4 M KFSI-DME and 4 M KFSI-DME-Co(OH)$_2$ under (a,b) 0 µC/cm^2 electrode potential and (c,d) −11.6 µC/cm^2 electrode potential.
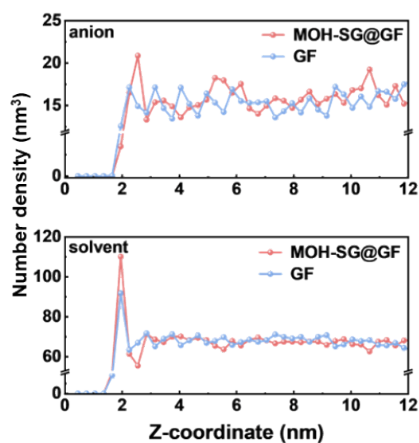
Fig. S13: MD simulations on EDL. Number density profiles of anions and solvents at the anode interface in MOH-SG@GF and GF system, as a function of distance from the K anode to electrolyte (with the application of a negative electrode potential).
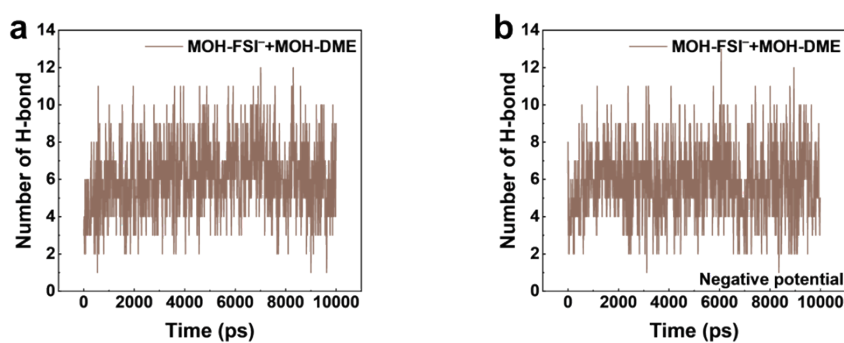
Fig. S14: MD simulations for H-bond. H-bond analysis under (a) 0 µC/cm^2 and (b) −11.6 µC/cm^2 electrode potential.
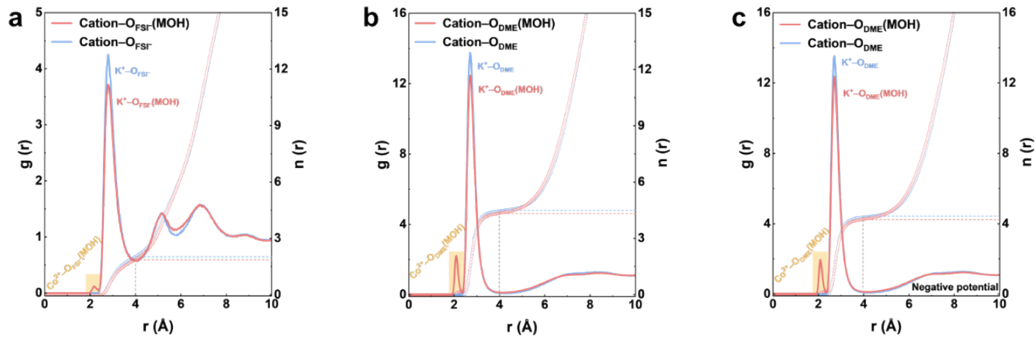
Fig. S15: MD simulations on solvation structure. RDFs [g(r), solid line] and CDFs [n(r), dashed line] of interactions between cations (K^+ and Co^{2+}) and (a) anions and (b,c) solvents, as a function of distance (r) from MD simulations in bare and MOH systems with an applied negative potential.
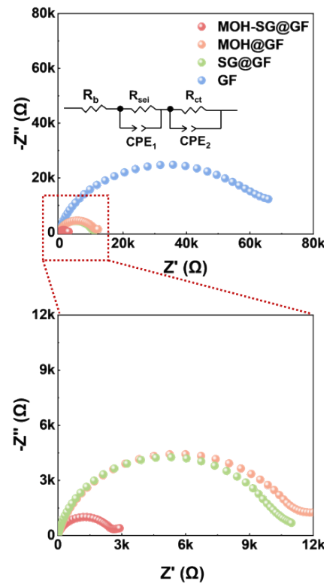
Fig. S16: Interfacial chemistry behavior. Nyquist plots of all samples at the initial state.
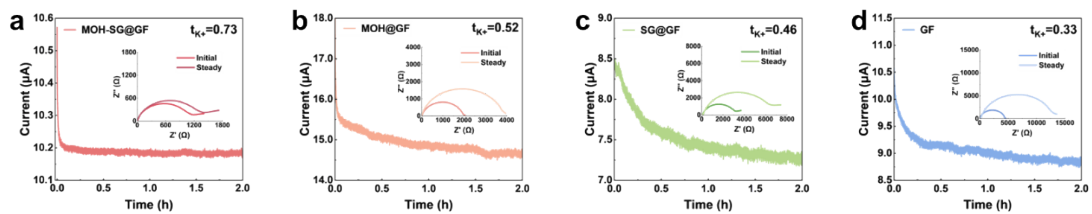
Fig. S17: Ion transfer properties. Chronoamperometry profiles of K‖K symmetric cells with different separators at a polarization of 10 mV (Inset: Nyquist plots before and after polarization).
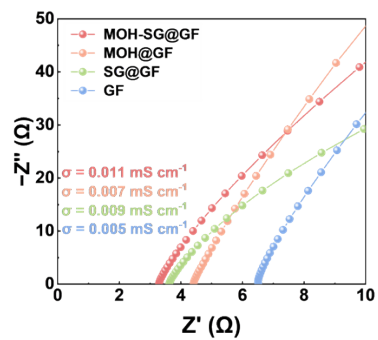
Fig. S18: Ion conductivity properties. Nyquist plots of symmetric cells with different separators.
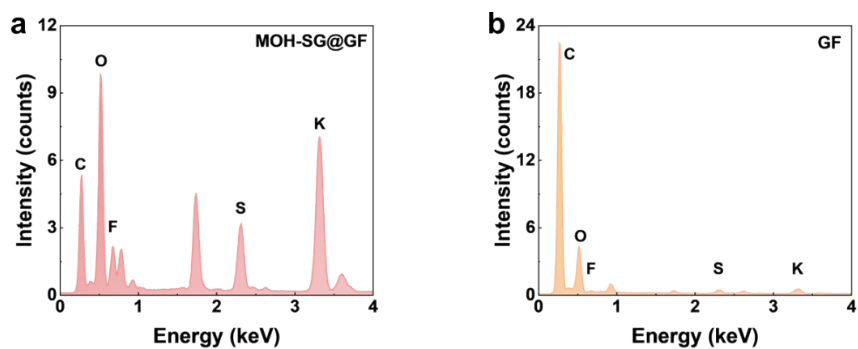
Fig. S19: Elemental features of the formed SEI. EDS profiles for (a) MOH-SG@GF and (b) GF systems.
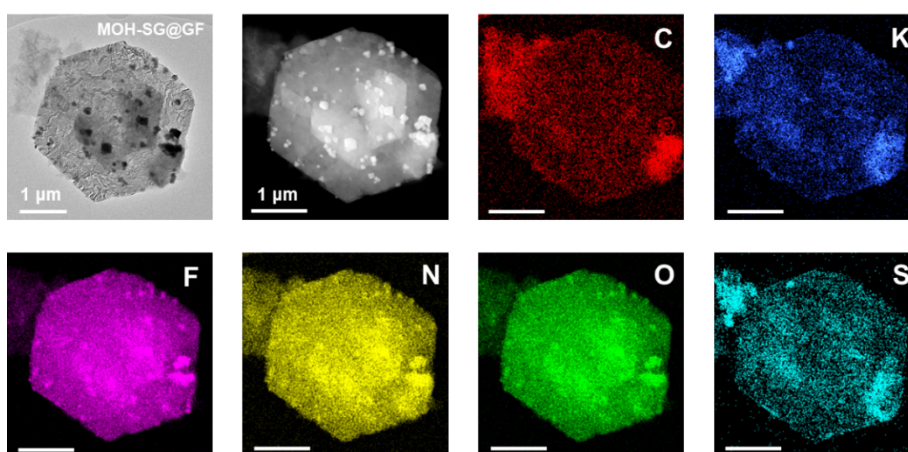
Fig. S20: Elemental maps of the formed SEI in MOH-SG@GF system.
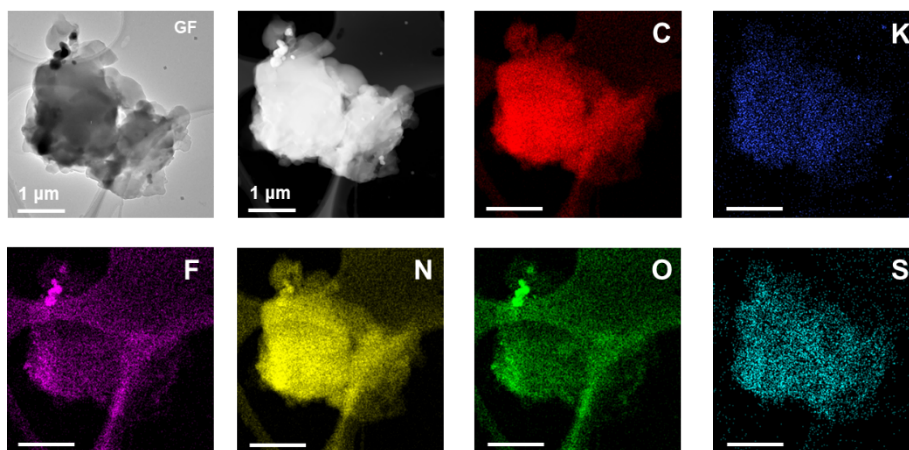
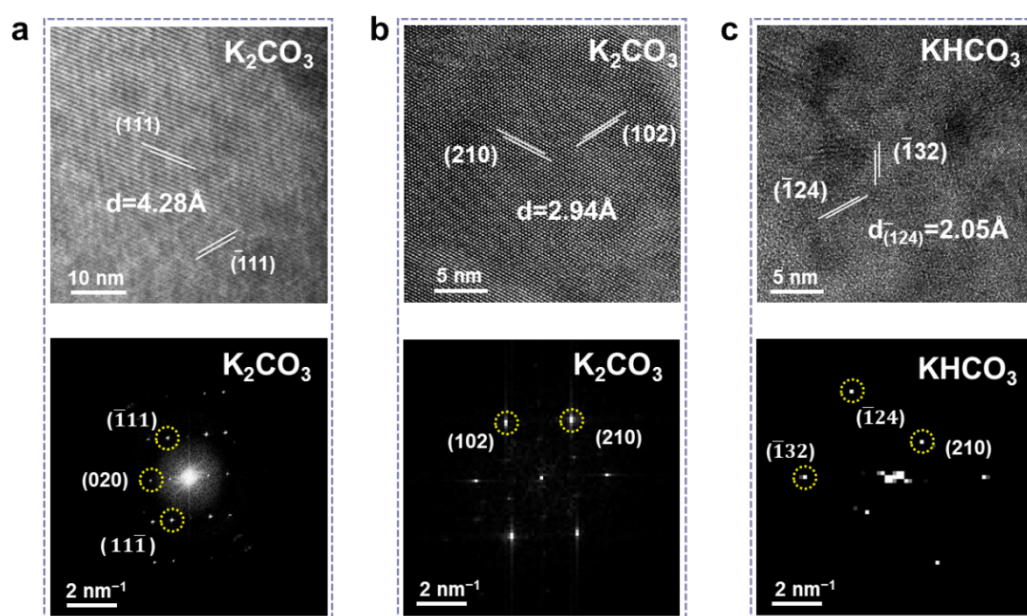**Fig. S21:** Elemental maps of the formed SEI in GF system.

Fig. S22: SEI component analysis by cryo-EM. Representative HRTEM images of (a,b) K_2CO_3 and (c) $KHCO_3$ phases and their indexed FFT patterns for MOH-SG@GF system derived SEI.
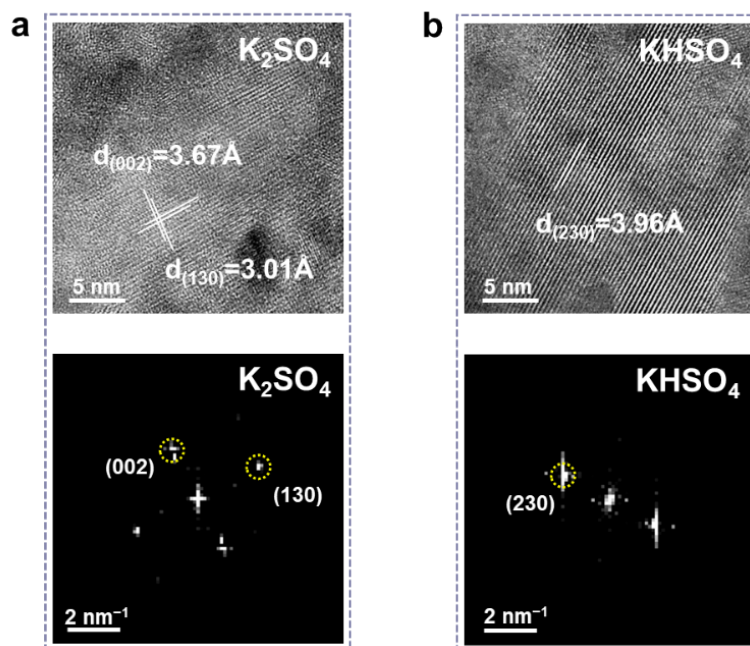
Fig. S23: SEI component analysis by cryo-EM. Representative HRTEM images of (a) K_2SO_4 and (b) $KHSO_4$ phases and their indexed FFT patterns for MOH-SG@GF system derived SEI.
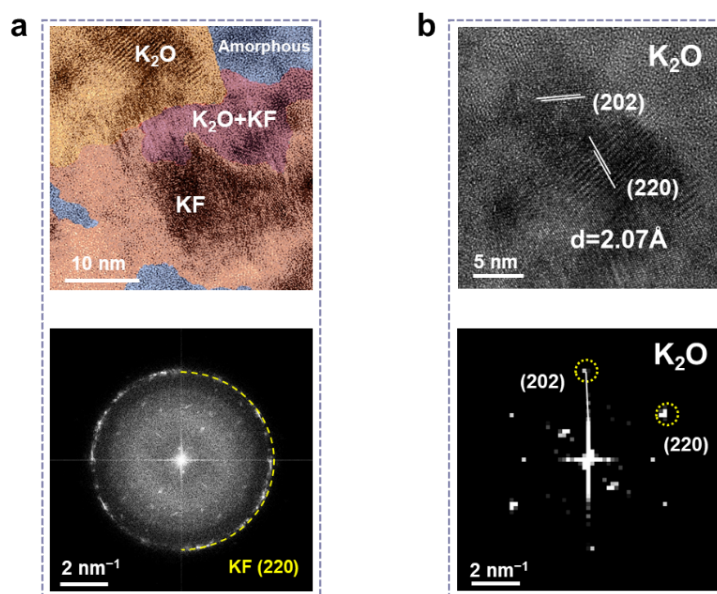

Fig. S24: SEI component analysis by cryo-EM. TEM view and the representative (a) KF and (b) K_2O phases and their corresponding FFT patterns for MOH-SG@GF system derived SEI.
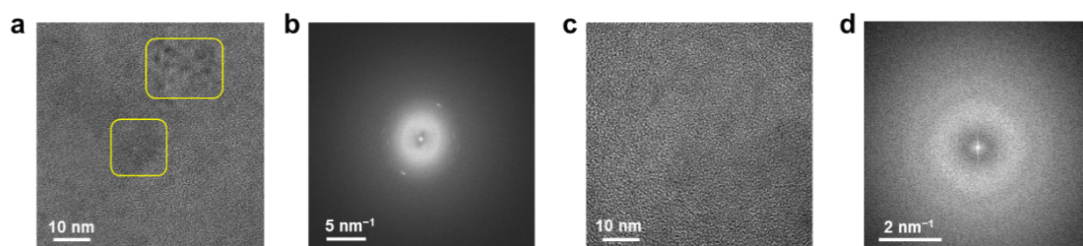
Fig. S25: SEI component analysis by cryo-EM. HRTEM images of bare GF system derived SEI, showing large-area amorphous phases with little crystalline regions (highlighted by yellow boxes).
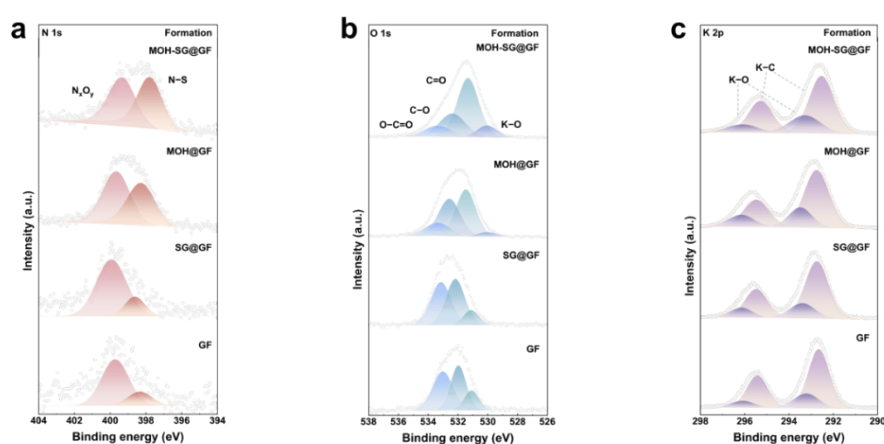

Fig. S26: SEI bonding configuration analysis. XPS (a) N $1s$, (b) O $1s$ and (c) K $2p$ spectra of the MOH-SG@GF system at the formation stage.
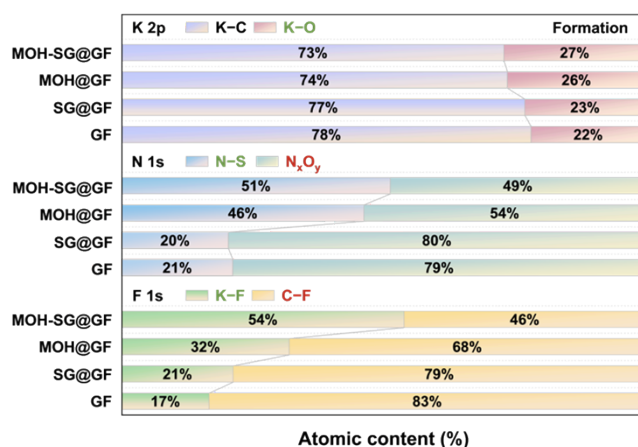

Fig. S27: SEI bonding configuration analysis. SEI chemical configurations and content percentages of all systems at the formation stage.
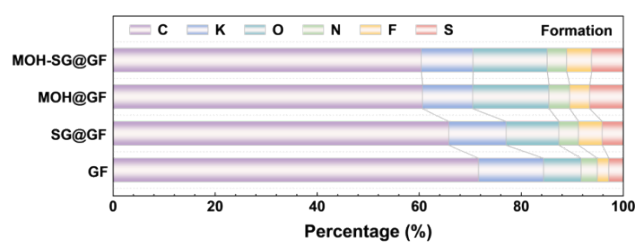
Fig. S28: SEI elemental analysis. SEI elemental content percentages of all systems at the formation stage.
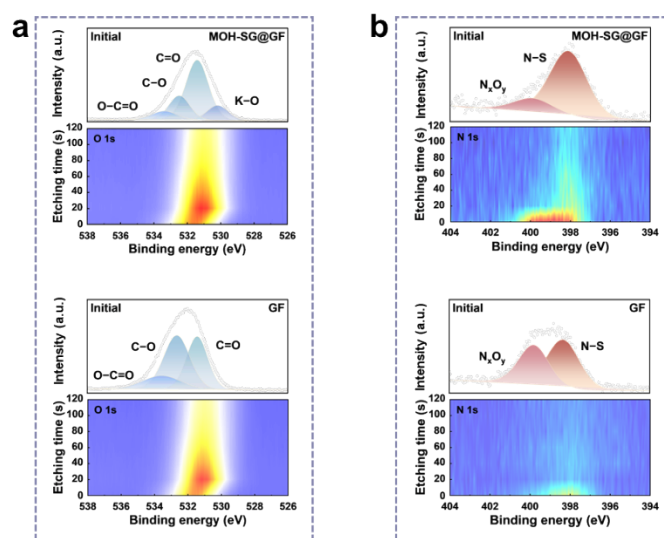

Fig. S29: SEI evolution analysis. XPS depth profiles of (a) O 1s and (b) N 1s for the MOH-SG@GF and GF systems. Each plot comprises two individual panels, *i.e.*, the spectrum at the initial etching stage (upper) and depth profile (lower).
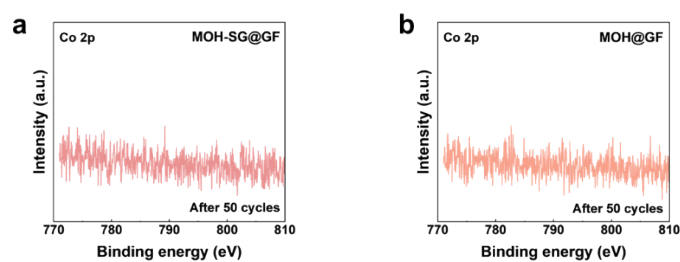

Fig. S30: XPS Co 2p spectra of the SEI layers formed in (a) MOH-SG@GF and (b) MOH-GF systems after 50 cycles, showing no trace of Co.
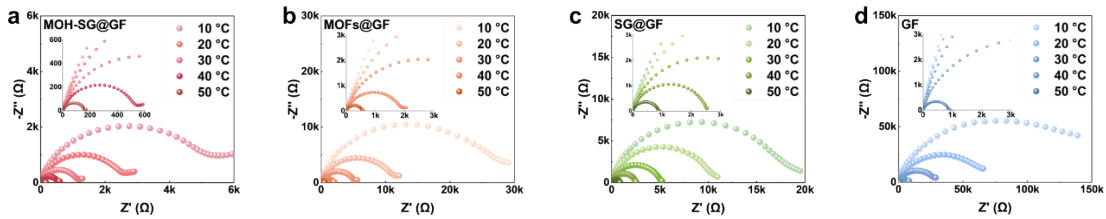
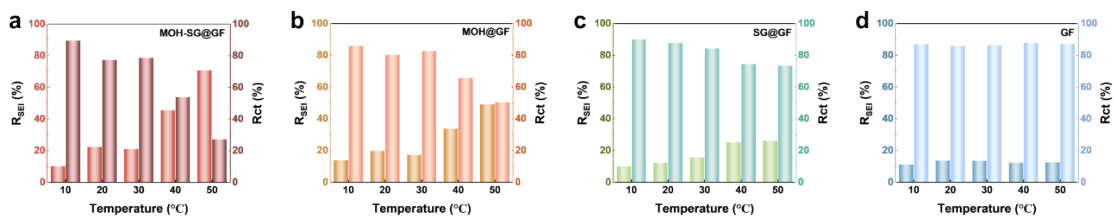**Fig. S31:** Nyquist plots of all separator systems at different temperatures.

Fig. S32: R_{SEI} and R_{ct} percentage profiles derived from the equivalent circuit model at a series of temperatures for all separator systems.
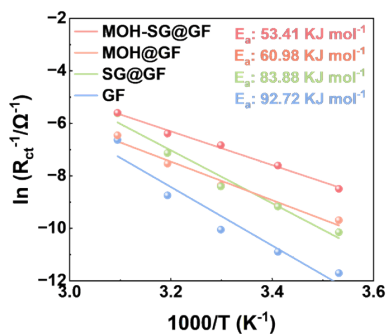

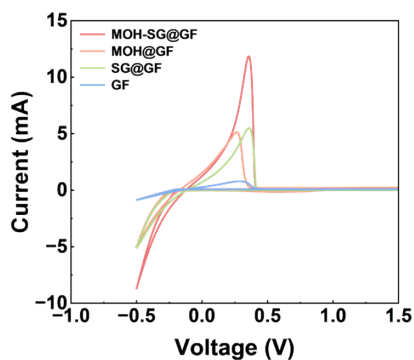**Fig. S33:** Interface dynamics analysis. Derived activation energy values.

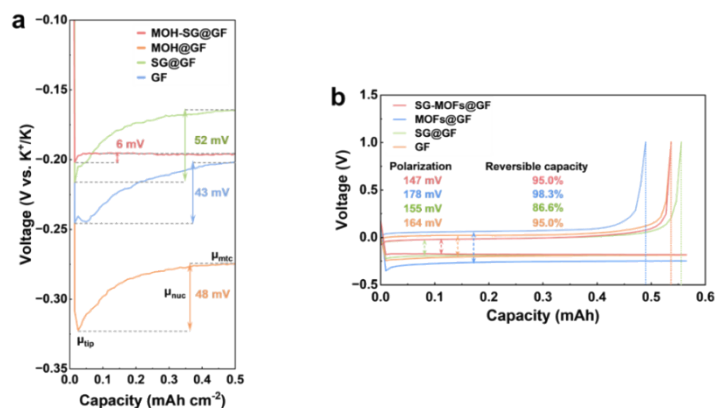**Fig. S34:** Interface dynamics analysis. CV curves for all systems.

Fig. S35: Interface chemistry analysis. (a) The voltage−capacity plots of all systems in asymmetric cell configuration at 0.5 mA cm⁻². (b) Electrochemical K plating/stripping curves of all systems at 0.5 mA cm⁻².
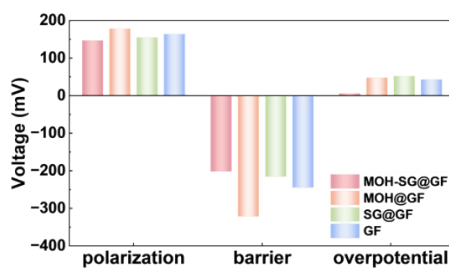

Fig. S36: Interface chemistry analysis. Histogram of polarization, nucleation barrier and overpotential information for all systems.
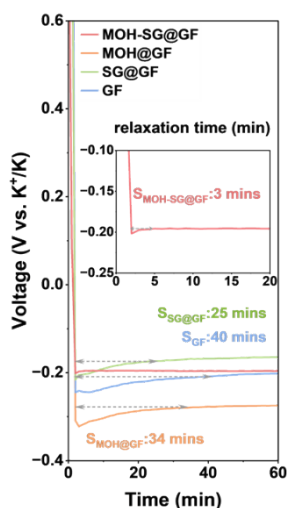
Fig. S37: Interface chemistry analysis. Comparison of relaxation time among all systems. The less relaxation time consumed represents the faster nucleation process.

Fig. S38: Cycling stability of asymmetric cells. Galvanostatic plating/stripping profiles for half-cells at 0.5 mA cm^{-2}/0.5 mAh cm^{-2} at (a) 1100−1200 h and (b) 1970−2000 h.
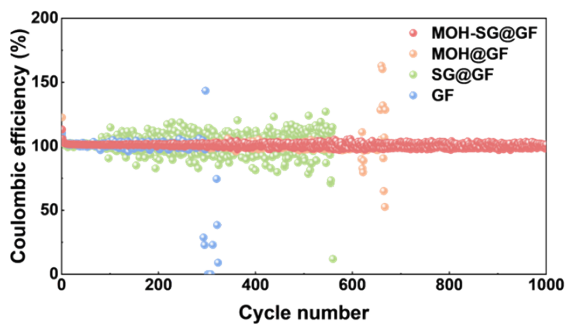
Fig. S39: Cycling stability of asymmetric cells. CE profiles from potassium plating/stripping.
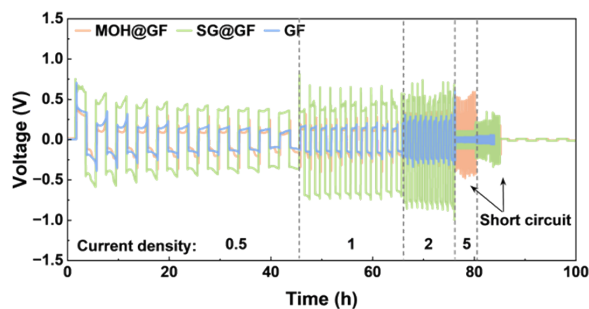
Fig. S40: Cycling stability of symmetric cells. Rate performances of symmetric cells equipped with different separators.

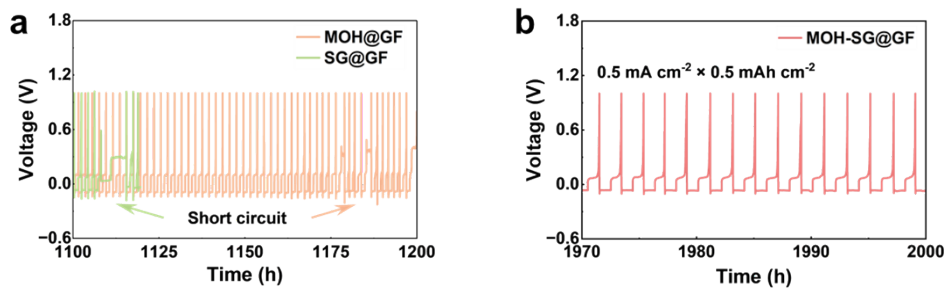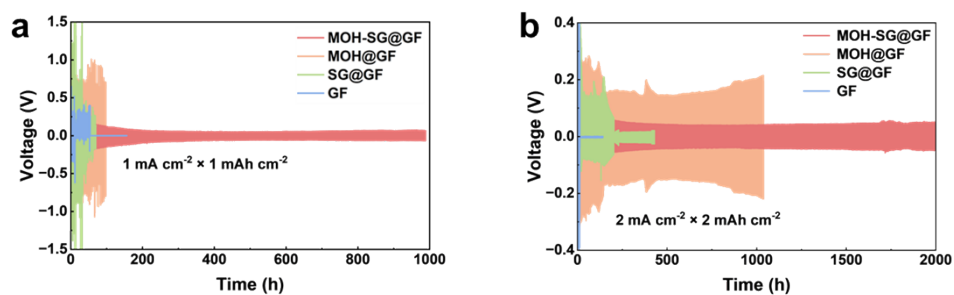**Fig. S41:** Cycling stability of symmetric cells. Galvanostatic profiles for symmetric cells at (a) 1.0 mA cm^{-2}/1.0 mAh cm^{-2} and (b) 2.0 mA cm^{-2}/2.0 mAh cm^{-2}.
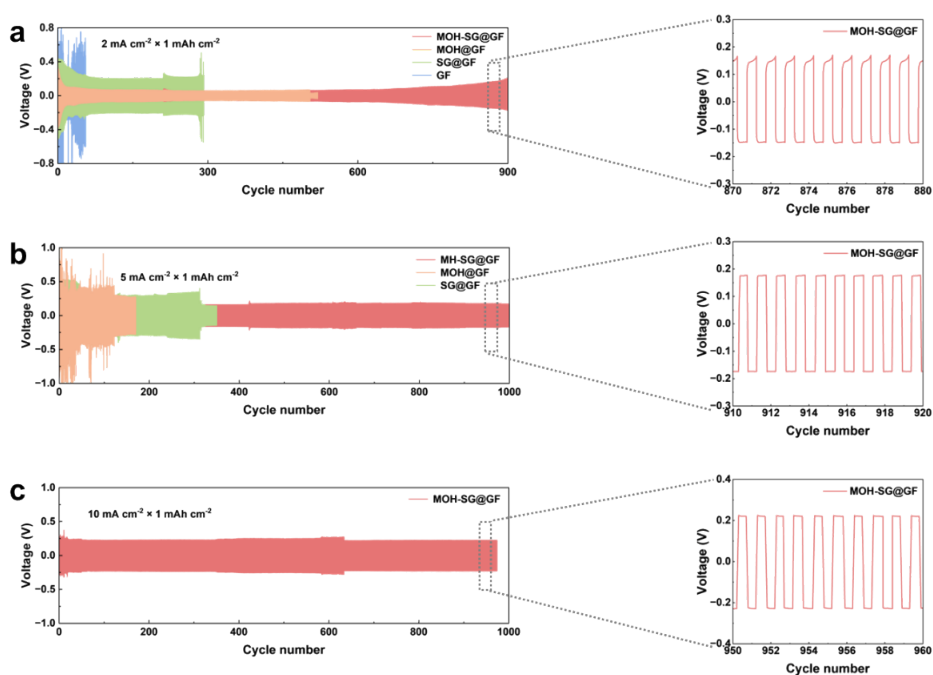
Fig. S42: Cycling stability of symmetric cells. Galvanostatic profiles for symmetric cells at (a) 2.0 mA cm^{-2}/1.0 mAh cm^{-2}, (b) 5.0 mA cm^{-2}/1.0 mAh cm^{-2} and 10 mA cm^{-2}/1.0 mAh cm^{-2} cycling with the corresponding enlarged view at the final state.
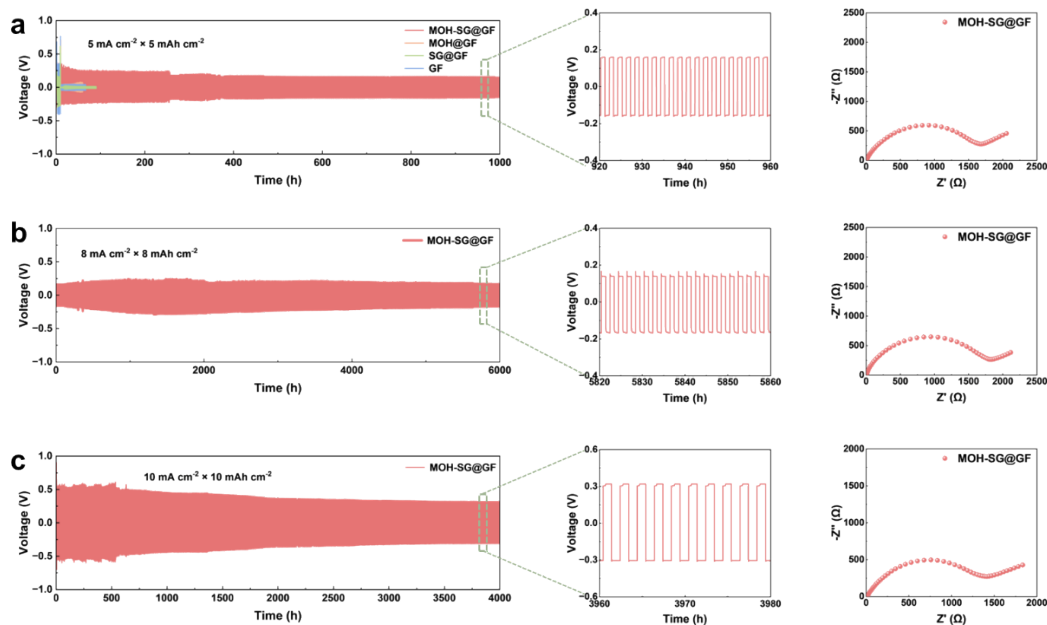
Fig. S43: Cycling stability of symmetric cells. Galvanostatic profiles for symmetric cells at (a) 5.0 mA cm^{-2}/5.0 mAh cm^{-2}, (b) 8.0 mA cm^{-2}/8.0 mAh cm^{-2} and 10 mA cm^{-2}/10 mAh cm^{-2} cycling with the corresponding enlarged view and Nyquist plots at the final state.
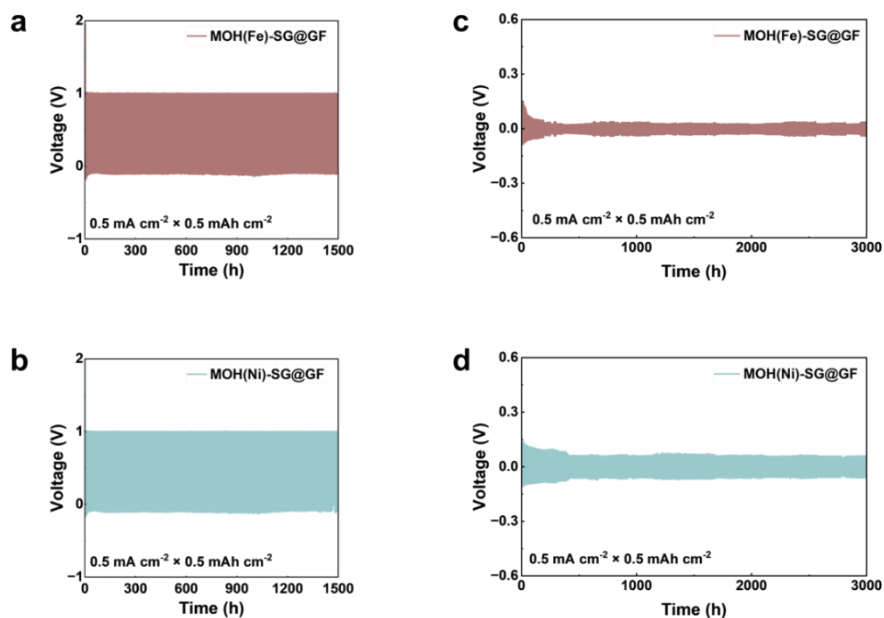
Fig. S44: The general employment of MOH. Cycling performance of asymmetric cells and symmetric cells based on (a,c) MOH(Fe)-SG@GF and (b,d) MOH(Ni)-SG@GF separators under 0.5 mA cm^{-2}/0.5 mAh cm^{-2}.
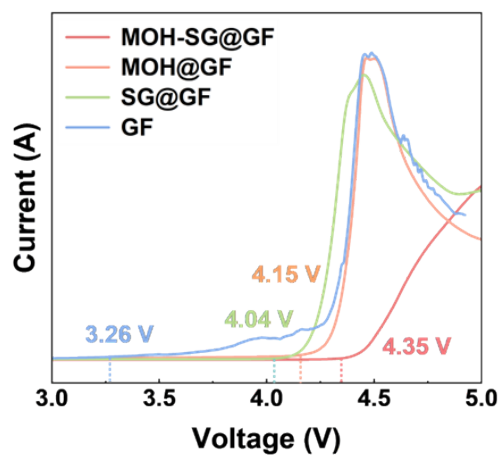
Fig. S45: Oxidation stability analysis. LSV curves of different separators.
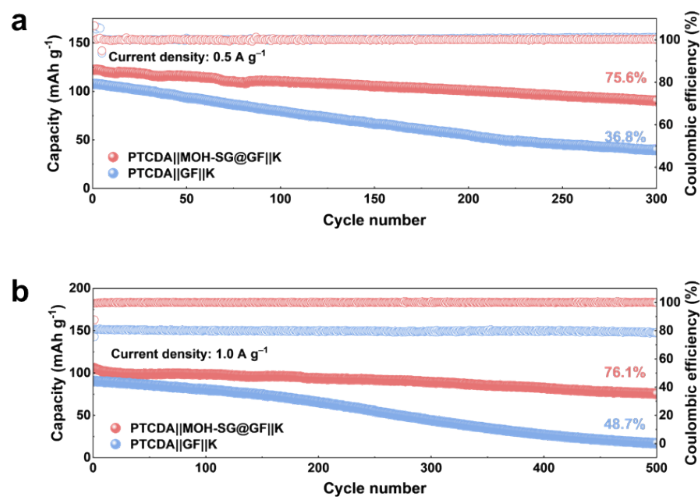
Fig. S46: Electrochemical performances of full cell. Cycling stability of PTCDA‖MOH-SG@GF‖K and PTCDA‖GF‖K cells at a current density of (a) 0.5 A g^{-1} and (b) 1.0 A g^{-1}.
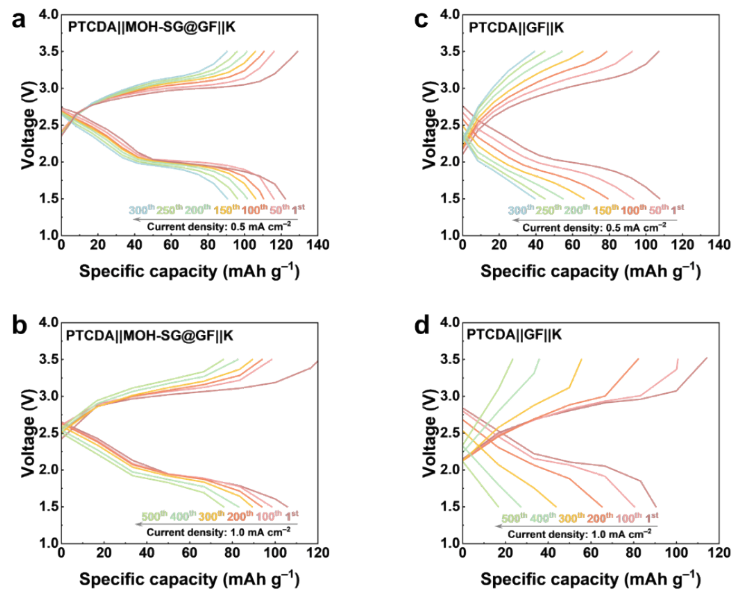
Fig. S47: Electrochemical performances of full cell. Charge-discharge curves of (a,b) PTCDA‖MOH-SG@GF‖K and (c,d) PTCDA‖GF‖K cells at different densities and cycles.
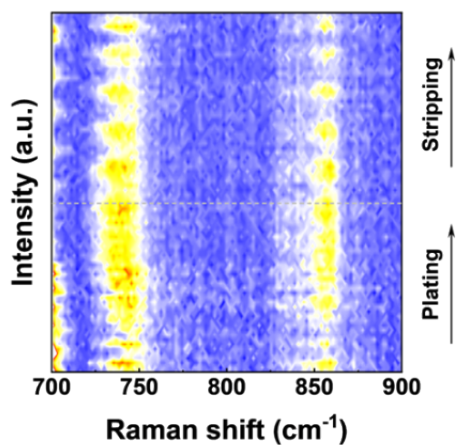
Fig. S48: Interface chemistry analysis. Contour plots of *operando* Raman profiles for K plating and stripping based on MOH-SG@GF.
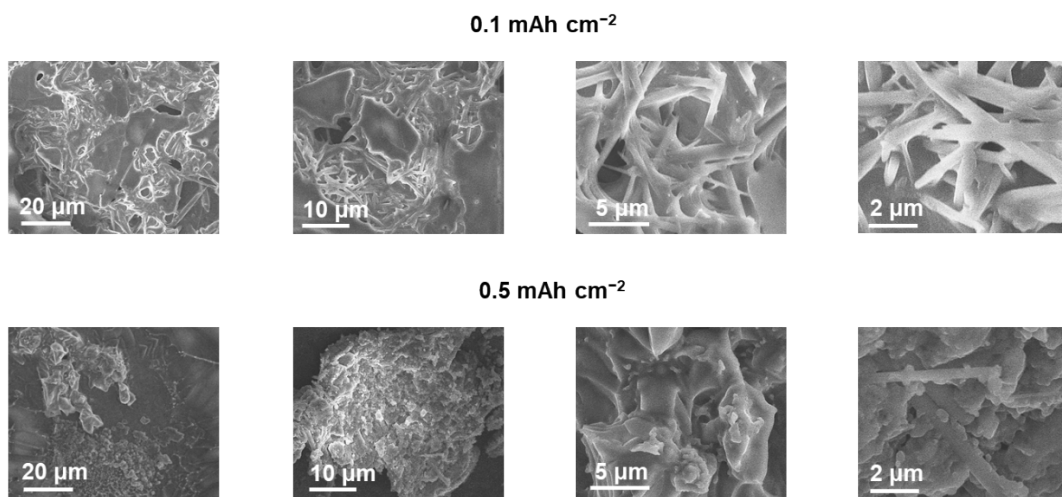
0.1 mAh cm^{-2}

0.5 mAh cm^{-2}

Fig. S49: K deposition morphology. SEM images of 0.1 (upper row) and 0.5 (lower row) mAh cm^{-2} K metal deposited on Al current collector based on GF separator.
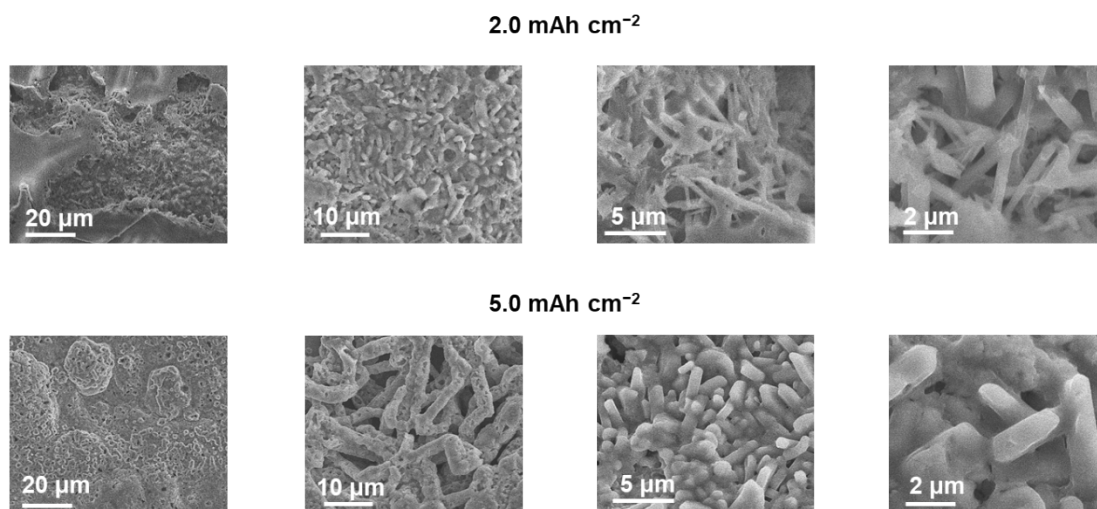
2.0 mAh cm^{-2}

5.0 mAh cm^{-2}

Fig. S50: K deposition morphology. SEM images of 2.0 (upper row) and 5.0 (lower row) mAh cm^{-2} K metal deposited on Al current collector based on GF separator.
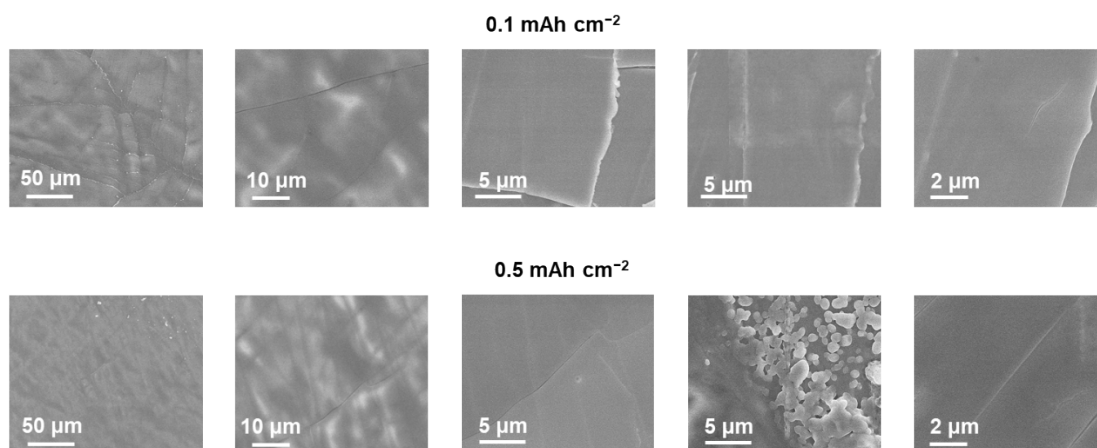
0.1 mAh cm⁻²

0.5 mAh cm⁻²

Fig. S51: K deposition morphology. SEM images of 0.1 (upper row) and 0.5 (lower row) mAh cm⁻² K metal deposited on Al current collector based on MOH-SG@GF separator.
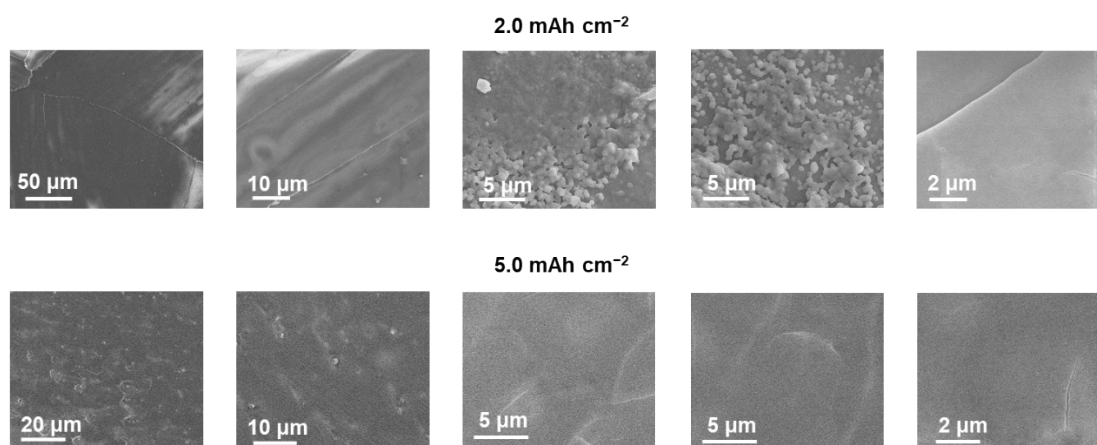
2.0 mAh cm⁻²

5.0 mAh cm⁻²

Fig. S52: K deposition morphology. SEM images of 2.0 (upper row) and 5.0 (lower row) mAh cm⁻² K metal deposited on Al current collector based on MOH-SG@GF separator.
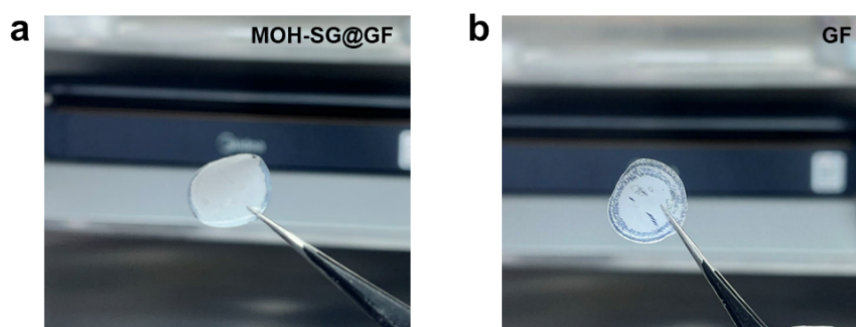
Fig. S53: Photos of disassembled coin cells. Polypropylene membrane dismantled from (a) MOH-SG@GF and (b) GF system.

Table S1. SEI content analysis. XPS quantitative analysis of the element percentage in SEIs derived from MOH-SG@GF and GF.

Atomic fraction (%)	Sample	C	N	O	F	S
	MOH-SG@GF	33.88	2.37	47.72	5.96	10.06
	GF	83.76	0.08	14.65	0.71	0.79

Table S2. Ion conductivity analysis. Summary of the fitted interface resistance values from Nyquist plots.

| R (Ω)	Sample	10 ℃	20 ℃	30 ℃	40 ℃	50 ℃
R_b	MOH-SG@GF	5.44	4.34	4.68	4.14	3.42
	MOH@GF	4.93	5.44	4.10	5.67	2.96
	SG@GF	9.13	4.89	4.41	3.79	2.95
	GF	3.85	4.35	2.92	2.29	2.97
R_{SEI}	MOH-SG@GF	556.40	585.40	274.40	249.90	116.60
	MOH@GF	4125.00	2336.00	935.20	647.10	269.80
	SG@GF	1775.00	1293.00	795.60	635.80	226.20
	GF	15059.00	8617.00	3669	873.50	109.10
R_{ct}	MOH-SG@GF	4894.00	2015.00	1024.00	295.60	44.73
	MOH@GF	25553.00	9589.00	4471.00	1254.00	276.40
	SG@GF	16140.00	9234.00	4304.00	1874.00	636.80
	GF	121710.00	53946.00	23187	6288.00	761.10

Table S3. Ion conductivity analysis. Percentage of fitted R_b, R_{SEI} and R_{ct} for all systems.

R (%)	Sample	10 ℃	20 ℃	30 ℃	40 ℃	50 ℃
R_b	MOH-SG@GF	0.10	0.17	0.36	0.76	2.08
	MOH@GF	0.02	0.05	0.07	0.30	0.54
	SG@GF	0.05	0.05	0.09	0.15	0.34
	GF	0.01	0.01	0.01	0.03	0.04
R_{SEI}	MOH-SG@GF	10.20	22.47	21.05	45.46	70.77
	MOH@GF	13.89	19.58	17.20	33.90	49.12
	SG@GF	9.90	12.28	15.59	25.29	26.12
	GF	11.01	13.77	13.66	12.19	12.49
R_{ct}	MOH-SG@GF	89.70	77.35	78.58	53.78	27.15
	MOH@GF	86.08	80.37	82.63	65.76	50.33
	SG@GF	90.05	87.68	84.32	74.55	73.54
	GF	87.07	86.22	86.32	87.77	87.16

Table S4. Electrochemical performance analysis. Performance comparison between MOH-SG@GF and other

Category	Material	Maximum current density (mA cm^{-2})	Maximum area capacity (mAh cm^{-2})	Maximum cyclic time (h)	Ref.
PMBs	**MOH-SG@GF**	**10**	**10**	**4000**	**This work**
		8	**8**	**6000**	
	PEP-NM	1	0.2	400	*Angew. Chem. Int. Ed. 2023*
	LiNO$_3$@PVDF	0.8	0.2	1700	*Adv. Energy Mater. 2023*
	AlF$_3$@PP	5	1	2000	*Adv. Mater. 2022*
	HPC	2	0.4	1000	*Adv. Energy Mater. 2022*
SMBs	AF5@GF	3	1	1800	*Adv. Mater. 2024*
	Co-NWS	2	1	500	*Adv. Mater. 2024*
	COF	20	1	2000	*Adv. Energy Mater. 2023*
	PTFE-GF	4	0.5	2700	*Adv. Energy Mater. 2023*
	NZSP@PP	2	0.5	1000	*Adv. Funct. Mater. 2023*
	S-3500	5	2.5	1000	*Adv. Mater. 2022*
LMBs	APV26	10	1	300	*Energy Storage Mater. 2024*
	TpPa-SO$_3$Li@PE	5	1	2600	*Adv. Funct. Mater. 2024*
	SnS$_2$@PP	20	5	2700	*Energy Storage Mater. 2023*
	LS	5	1	1200	*Adv. Mater. 2023*
	PCS	15	30	300	*Energy Environ. Sci. 2023*
	AP3	10	10	500	*Energy Storage Mater. 2023*
	f-PTC	10	3	1000	*Energy Storage Mater. 2022*
	COF/PVDF	5	5	700	*ACS Energy Lett. 2022*
	PVA/LRD@PP	30	15	2500	*Energy Storage Mater. 2021*
	GO-g-PAM@PP	20	5	2500	*Nature Commun. 2019*

functional separators reported in previous literatures.

Table S5. MD simulations details. The repulsion and attraction interaction in non-bond terms of OPLS force field.

	K$^+$	Co^{2+}	K
Sigma	4.93463e-01	0.2559	4.16139E-01
Epsilon	1.37235e-03	0.0586	1.45302E+01

Table S6. MD simulations details. The repulsion and attraction interaction in non-bond terms of OPLS force field.

OH$^-$	O	H
Sigma	3.12000e-01	0.00000e+00
Epsilon	7.11280e-01	0.00000e+00

Table S7. MD simulations details. The repulsion and attraction interaction in non-bond terms of OPLS force field.

FSI$^-$	S	F	O	N
Sigma	3.55000e-01	2.94000e-01	2.90000e-01	3.25000e-01
Epsilon	1.04600e+00	2.55224e-01	5.85760e-01	7.11280e-01

Table S8. MD simulations details. The repulsion and attraction interaction in non-bond terms of OPLS force field.

DME	O	C	H
Sigma	2.90000e-01	3.50000e-01	2.50000e-01
Epsilon	5.85760e-01	2.76144e-01	1.25520e-01

Supplementary Reference:

1. L. Martínez, R. Andrade, E. G. Birgin and J. M. Martínez, *J. Comput. Chem.*, 2009, **30**, 2157-2164.
2. J. M. Martínez and L. Martínez, *J. Comput. Chem.*, 2003, **24**, 819-825.
3. B. C. Yeo, H. Jung, H. W. Lee, K.-S. Yun, H. Kim, K.-R. Lee and S. S. Han, *J. Phys. Chem. C*, 2017, **121**, 23268-23275.
4. Berk Hess, Carsten Kutzner, David van der Spoel and E. Lindahl, *J. Chem. Theory Comput.*, 2008, **4**, 435-447.
5. T. Darden, D. York and L. Pedersen, *J. Chem. Phys.*, 1993, **98**, 10089-10092.